Discovery of two new Cu-Sn chalco-halides for potential solar absorber applications

Brinda Kuthanazhi[1], Debalina Banerjee[2], Dmitry Maslennikov[2], Andrij Vasylenko[1], Jan P. Scheifers[1], Cara J. Hawkins[1], Daniel Ritchie[1], Craig M. Robertson[1], Marco Zanella[1], Troy D. Manning[1], Luke M. Daniels[1], Marina Filip[2], Matthew S. Dyer[1], Laura Herz[2], John B. Claridge[1], and Matthew J. Rosseinsky*[1].

[1]Department of Chemistry, Materials Innovation Factory, University of Liverpool, Liverpool L7 3NY, U.K.

[2]Department of Physics, University of Oxford, Oxford OX1 3PU, U.K.

Supplementary Information

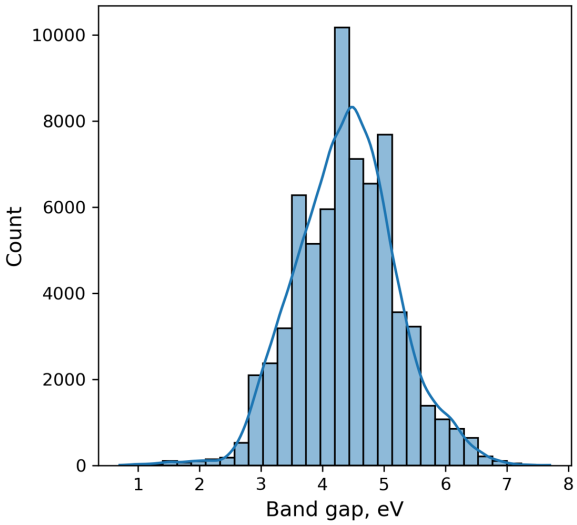

Figure S1 Distribution of finite bang gap values in the 68823 experimentally reported compounds in MPDS. Use of this data for training introduces a bias towards elemental combinations exhibiting a finite band gap.

Table S1 List of reported ternary compounds within the Cu-Sn-S-I phase field that satisfies the oxidation states Cu^{1+}, Sn^{2+}, S^{2-}, and I^{1-}. There are only five ternary compounds and no quaternary compounds known, showing the under explored nature of this phase field.

Compounds
Cu_3SI
Cu_2SnI_4
$CuSnI_3$
Sn_4SI_6
Sn_2SI_2

Structure comparisons:

Table S2. Bond valence sum calculated for various cations in $CuSn_2SI_3$ and $Cu_{0.35}Sn_{5.29}S_2I_7$. All calculations are based on the distances shown in the various cation coordination environments in Figure 2(b) and Figure 3(b). The Cu1, Cu2, and Sn00 sites in $Cu_{0.35}Sn_{5.29}S_2I_7$ are partially occupied which accounts for the less accurate values.

Compound	**Atom**	**BVS**
$CuSn_2SI_3$	Cu	0.9
	Sn1	1.89
	Sn2	1.91
$Cu_{0.35}Sn_{5.29}S_2I_7$	Cu1	0.84
	Cu2	0.87
	Sn00	2.29
	Sn1	1.90
	Sn2	1.93

Table S3 Bond valence sum for the different cations in $CuSn_2SI_3$ and $Cu_{0.35}Sn_{5.29}S_2I_7$ without considering the longer Sn–I distances within the $Sn_4S_2I_4$ units of each structure. This gives poorer agreement with expected oxidation states, indicating the presence of the longer Sn-I distances.

Compound	Atom	BVS
$CuSn_2SI_3$	Cu	0.9
	Sn1	1.76
	Sn2	1.77
$Cu_{0.35}Sn_{5.29}S_2I_7$	Cu1	0.84
	Cu2	0.87
	Sn00	2.29
	Sn1	1.73
	Sn2	1.79

Table S4 Bond valence sum values calculated for the disordered compound, $Cu_{0.35}Sn_{5.29}S_2I_7$, with a hypothetical Sn octahedra with no distortion. Hypothetical structure with no distortion gives poorer agreement to expected Sn oxidation state of 2+.

Compound	Atom	BVS
$Cu_{0.35}Sn_{5.29}S_2I_7$ (hypothetical without distortions)	Cu1	0.88
	Cu2	0.90
	Sn00	2.34
$Cu_{0.35}Sn_{5.29}S_2I_7$ (experimental)	Cu1	0.84
	Cu2	0.87
	Sn00	2.29

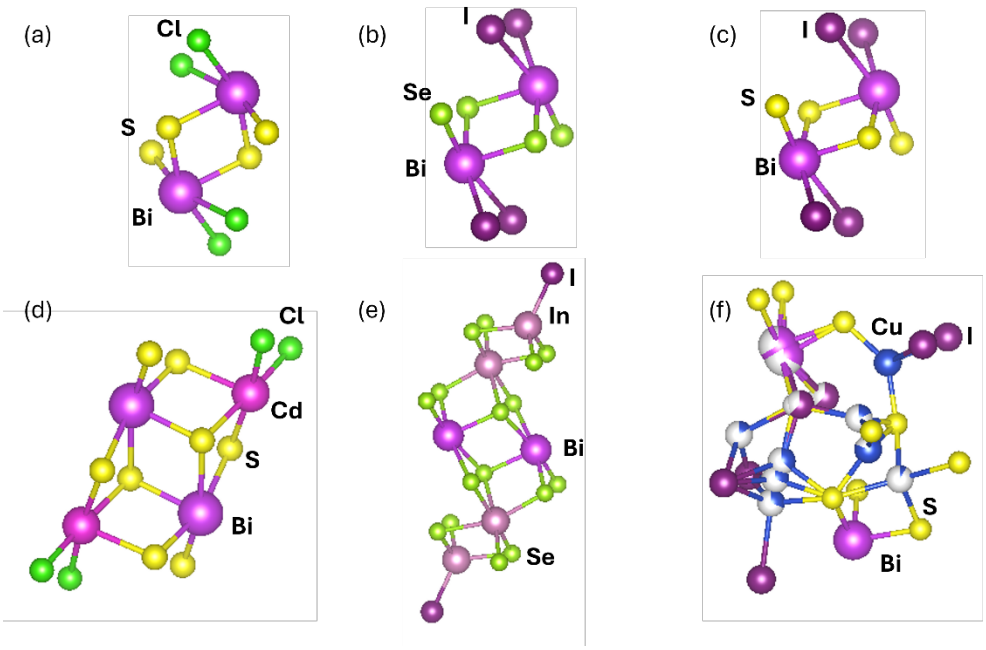

Figure S2 Comparison of the structural units in different quaternary chalco-halides. (a), (b), (c) show the structures of ternary bismuth chalco-halides BiSCl, BiSeI, and BiSI (d), (e), (f) show the extended unit formed by the incorporation of a second cation, in $CdBiS_2Cl$, In_2BiSe_4I, and $Cu_3Bi_2S_3I_3$ respectively.

Table S5 The list of quaternary chalco-halides with d^{10} and s^2 cations. Compounds containing Bi^{3+} and O^{2-} are not listed.

Compound	Space group	Structural units	Dimensionality	Band gap	Ref.
$Ag_5SbS_3I_2$	Pnnm (58)	$[SbS_3]$, $[AgS_2I]$, $[AgS_2I_2]$	3D	-	[1]
$Cu_5SbS_3I_2$	Pnnm (58)	$[SbS_3]$, $[CuS_2I]$, $[CuS_2I_2]$	3D	'red-orange'	[2]
$Hg_2PbS_2I_2$	P4/mbm (127)	$[HgS_2I_2]$, $[PbS_4I_3]$	3D	-	[3]
$Hg_2SnS_2Br_2$	$P2_1/c$ (14)	$[[HgS_3]$, $[HgS_2]$, $[SnS_2Br_3]$	3D	-	[4]
$CdSnSBr_2$	Cmcm (63)	$[CdBr_4S_2]$, $[SnS_2Br_2]$	2D	2.72 eV	[5]
$CdSnSCl_2$	Cmcm (63)	$[CdCl_4S_2]$, $[SnS_2Cl_2]$	2D	2.87 eV	[5]

Table S5 gives the list of known quaternary chalco-halides with an s^2 and a d^{10} cation. Bi containing compounds and oxyhalides are not included. Most structures are three dimensional with $CdSnSX_2$ (X=Cl, Br) being the exceptions. There is little known about the band gap and the nature of band gap for most of the other compounds.

Synchrotron powder XRD at 100 K:

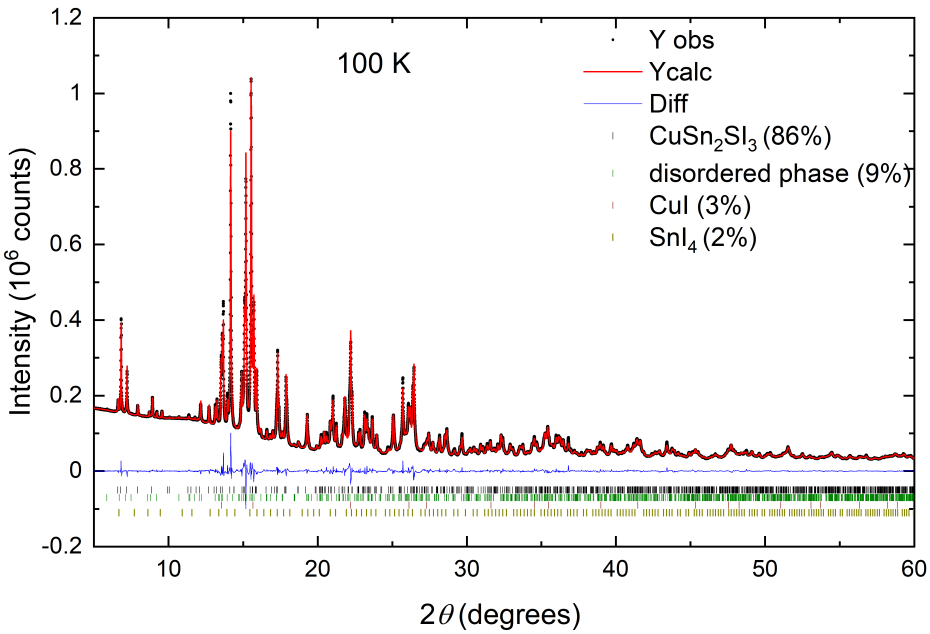

Figure S3 Synchrotron powder x-ray diffraction pattern of $CuSn_2SI_3$ sample measured at 100 K. The parameters from the Rietveld refinement are given in Table S16 .

Elemental analysis:

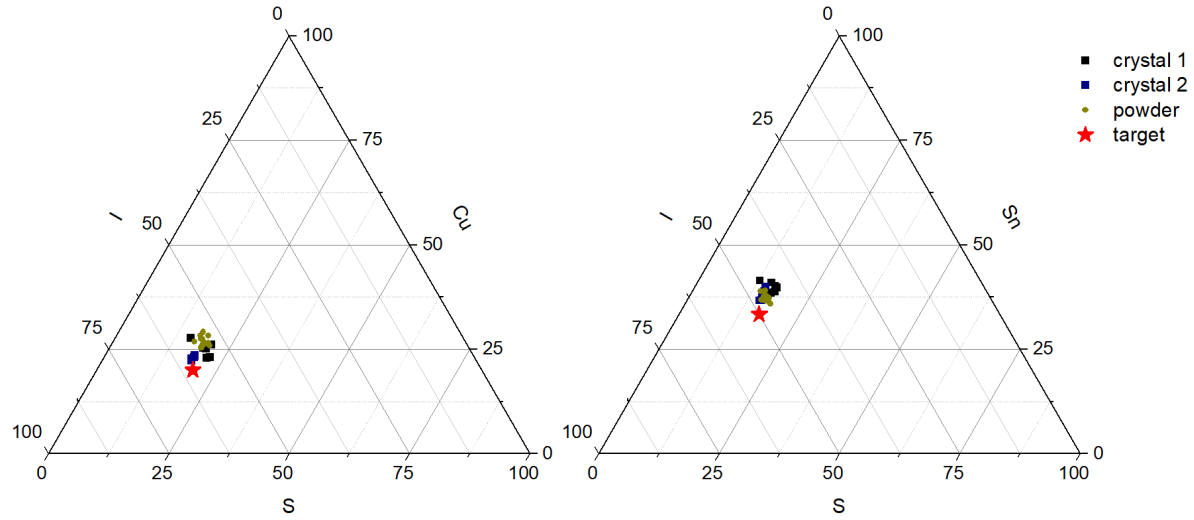

Figure S4 The elemental composition data on $CuSn_2SI_3$ samples obtained from SEM-EDX spectroscopy, presented as ternary plots of (a) Cu-S-I and (b) Sn-S-I. The red star shows the target composition of $CuSn_2SI_3$. The black and blue squares are from measurements on multiple single crystals. Yellow circles are from ball milled powder sample.

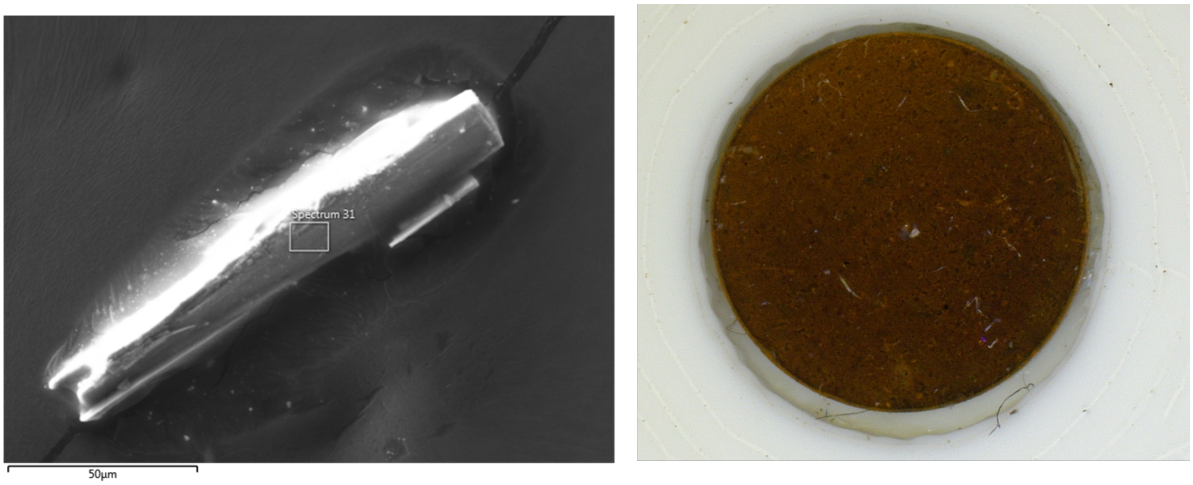

Figure S5 Left: SEM image of a single crystal on which EDX was measured. Right: Image of a 5 mm diameter pellet of $CuSn_2SI_3$, on which THz spectroscopy measurements were performed.

X-ray photoemission Spectroscopy

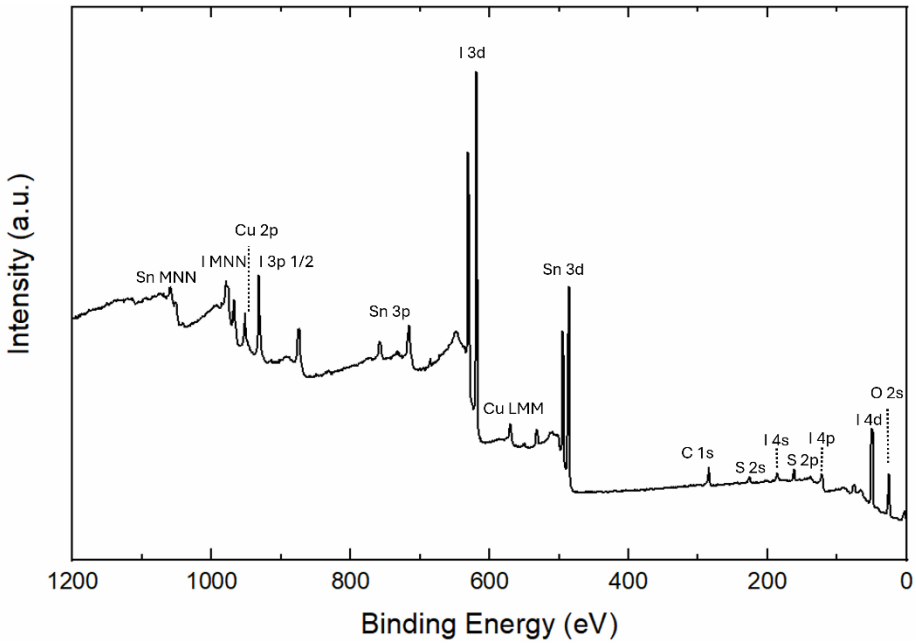

Figure S6 XPS survey spectrum for $CuSn_2SI_3$ powder sample.

All elements expected are identified in the XPS survey spectrum. Presence of O 2s indicates slight oxidation of the sample during transit/measurement.

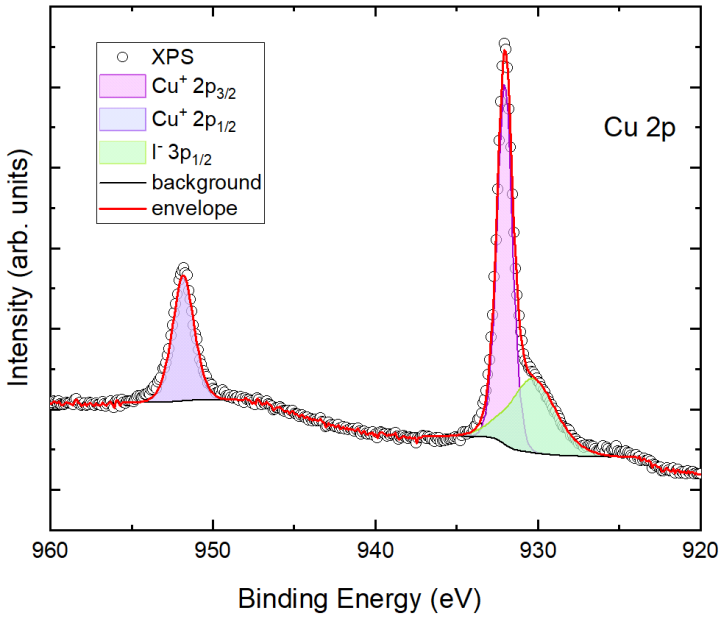

Figure S7 Core level spectrum of Cu^+ in $CuSn_2SI_3$ powder sample with the peaks corresponding to $2p_{3/2}$ and $2p_{1/2}$ fitted. The broad peak in green corresponds to $3p_{1/2}$ level from I^- anion.

Table S6 The binding energy and full width half maximum (FWHM) values obtained from fitting the core level XPS spectrum of Cu^+ 2p levels and I^- 3p levels. Comparison with values from the literature for $CuBiSeCl_2$ is also given.

	Measured		**Literature**[17]	
Cu	**Binding Energy (eV)**	**FWHM**	**Binding Energy (eV)**	**FWHM**
Cu 2p 3/2	932.04	1.09	932.32	1.18
Cu 2p 1/2	951.82	1.56	952.1	1.88
	Δ =19.78		Δ = 19.8	
I				
I 3p 1/2	930.31	3.34	930	-

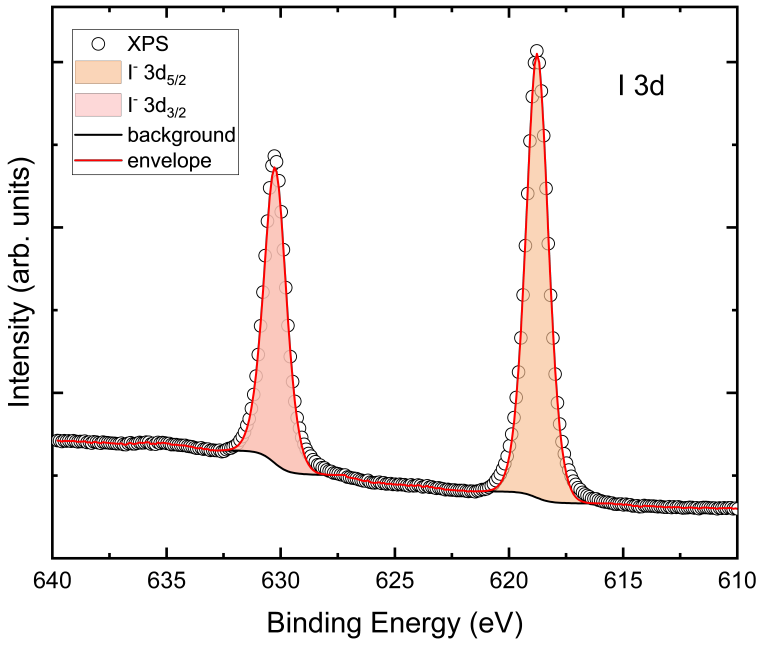

Figure S8 Core level spectrum of I^- 3d levels in $CuSn_2SI_3$ powder sample.

Table S7 The binding energy and full width half maximum (FWHM) values obtained from fitting the core level XPS spectrum of I^- and comparison with values from the literature on KI.

I	Measured		Literature[18]	
	Binding Energy (eV)	**FWHM**	**Binding Energy (eV)**	**FWHM**
I 3d 5/2	618.76	1.16	619.3	-
I 3d 3/2	630.24	1.16	630.8	-
	Δ = 11.48		Δ = 11.5	

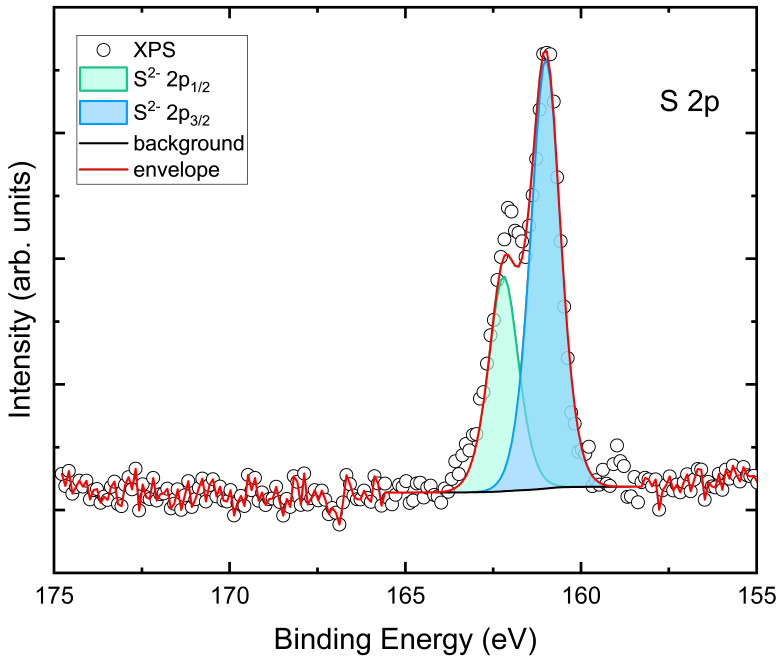

Figure S9 Core level spectrum of S^{2-} 2p levels in $CuSn_2SI_3$.

Table S8 The binding energy and full width half maximum values obtained from fitting the core level XPS spectrum of S^{2-} and comparison with values from the literature for SnS.

S	**Measured**		**Literature**[19]	
	Binding Energy (eV)	**FWHM**	**Binding Energy (eV)**	**FWHM**
S 2p 1/2	162.20	1.00	162.25	-
S 2p 3/2	161.00	1.00	161.07	-
	Δ = 1.20		Δ = 1.18	

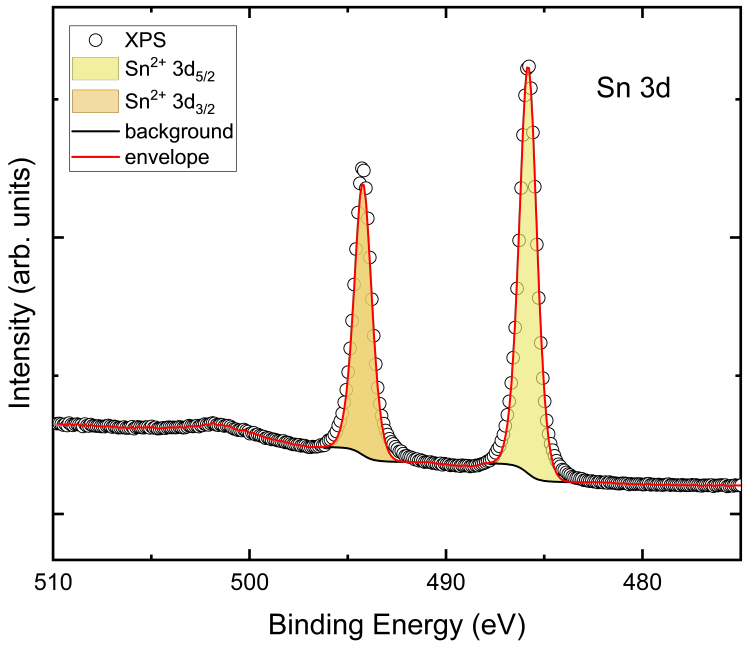

Figure S10 Core level spectrum of 3d levels of the Sn^{2+} cation in $CuSn_2SI_3$ sample.

Table S9 The binding energy and full width half maximum values obtained from fitting the core level XPS spectrum of Sn^{2+} and comparison with values from the literature for SnS.

Sn	**Measured**		**Literature**[19]	
	Binding Energy (eV)	**FWHM**	**Binding Energy (eV)**	**FWHM**
Sn 3d 5/2	485.82	1.05	485.57	0.81
Sn 3d 3/2	494.23	1.05	493.98	-
	Δ = 8.41		Δ = 8.41	

UV-Vis Spectroscopy:

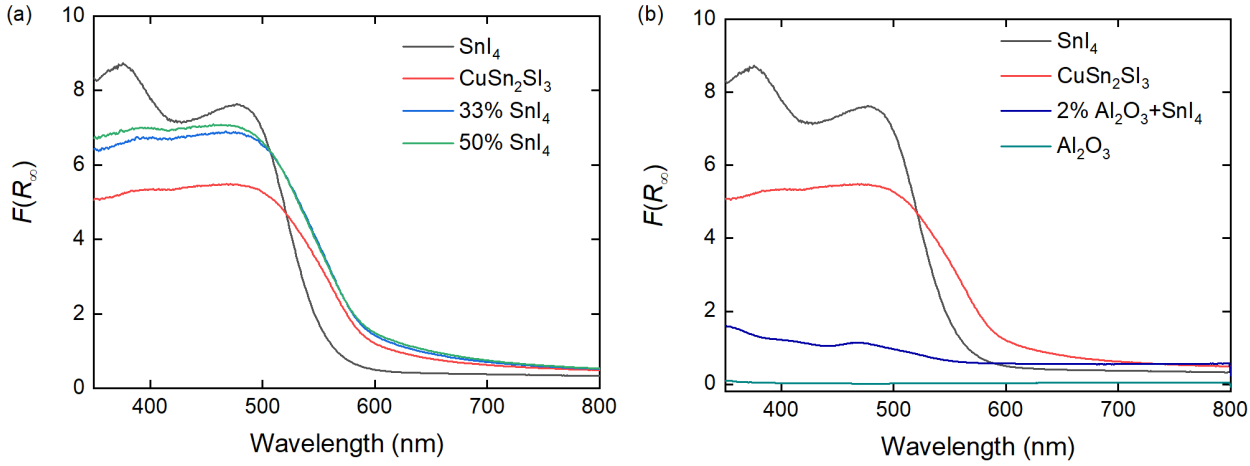

Figure S11 (a) Pseudo absorbance spectra for SnI_4, $CuSn_2SI_3$, and mixtures of $CuSn_2SI_3$ and SnI_4. (b) Pseudo absorbance spectra for SnI_4, $CuSn_2SI_3$, Al_2O_3, and a mixture of Al_2O_3 and SnI_4.

The diffuse reflectance spectra measured for the $CuSn_2SI_3$ sample was shown in the main text. However, the sample has impurities present in it which makes it difficult to interpret the absorption data and to obtain the band gap. CuI has a wide band gap of ~3 eV[6,7] and should not affect the absorption edge at ~ 500 nm. However, SnI_4 is known to have a band gap ~2.18 eV,[8] hence we need to eliminate the possibility that the absorption edge is coming entirely from the small amount of SnI_4 impurity. This can be the case for strongly absorbing impurities in weakly absorbing sample. To clarify this, we measure absorption spectra for SnI_4, and two samples with 50 weight percent and 33 weight percent SnI_4 mixed with the as synthesised $CuSn_2SI_3$ sample. We also measured 2 weight percent of SnI_4 mixed with Al_2O_3, which is a wide band gap material with no absorption in the range we measured, to investigate the contribution to absorption coming from the presence of a comparable amount of SnI_4 impurity as present in our samples. These are shown in Figure S11, plotted as the Kubelka-Munk transformed reflectance.

While SnI_4 has a larger pseudo-absorbance it is not significantly larger than '$CuSn_2SI_3$' sample. If the absorption spectrum of $CuSn_2SI_3$ sample was entirely coming from 2% SnI_4 impurity precent, 50 weight percent and 33 weight percent SnI_4 would have led to huge increases in absorption which is not observed. The lack of a proportionally large absorbance for pure SnI_4, and mixed SnI_4 and $CuSn_2SI_3$ samples eliminates the possibility of absorption coming entirely from SnI_4. Notably, the higher energy (~400 nm) peak present in SnI_4, while visible, is not prominent in any of the other three samples. Furthermore, the absorption edge is shifted towards higher wavelengths (lower energies) in all three samples as compared to SnI_4. All of this indicate that while the absorption edge is influenced (possibly broadened) by the presence of SnI_4, it is not coming entirely from SnI_4. This is further confirmed by the absorption spectrum of 2% SnI_4 added to Al_2O_3, shown in Figure S11 (b), which gives a much lower absorbance than all the samples with $CuSn_2SI_3$ and has a broad absorption edge consistent with that of pure SnI_4. This is still at a slightly lower wavelength than what is observed in $CuSn_2SI_3$. This suggests that the measured absorption spectrum is primarily coming from a mixture of $CuSn_2SI_3$ and $Cu_{0.35}Sn_{5.29}S_2I_7$ and has a band gap slightly below that of SnI_4.

Electronic band structure calculations:

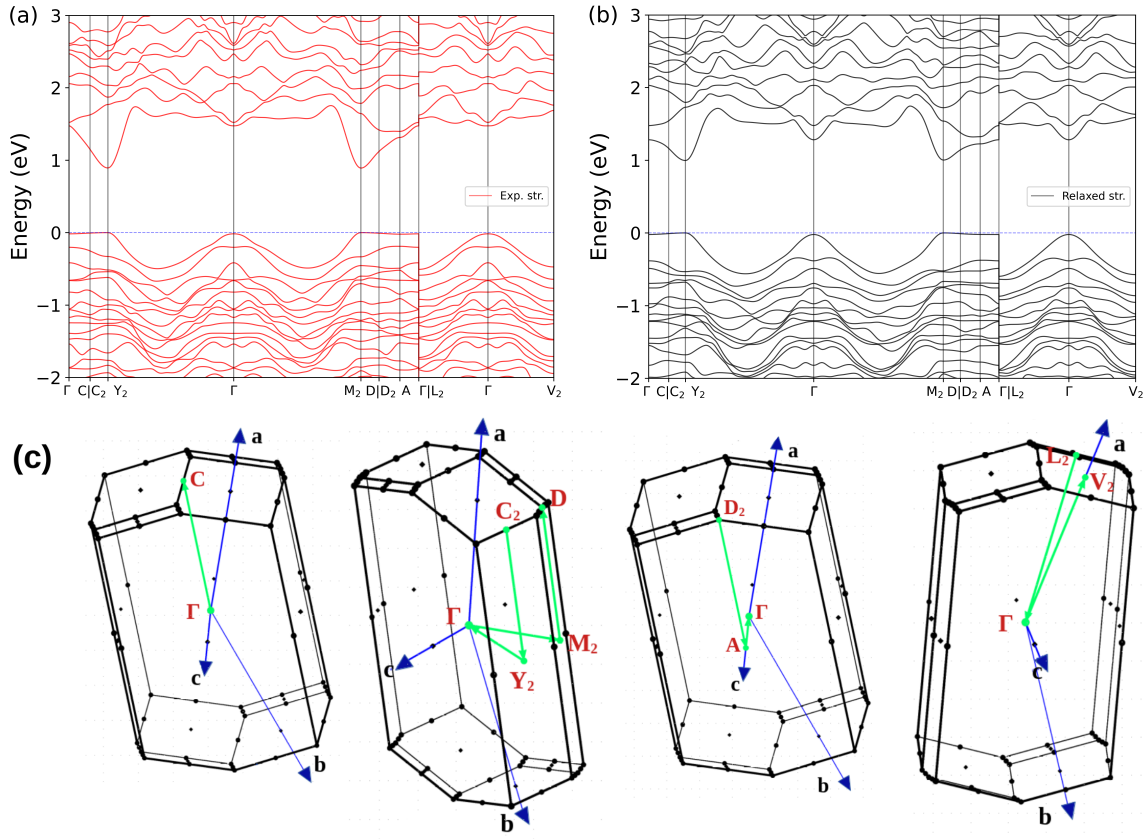

Figure S12 The electronic band structure for the ordered phase of $CuSn_2SI_3$ calculated for (a) the experimental structure, and (b) the- relaxed structure using DFT (PBE)+SOC and along the full path Γ-C|C_2 -Y2- Γ -M_2-D |D_2-A-Γ|L_2 -Γ-V_2 in the Brillouin zone, where the high-symmetry points for this monoclinic structure reported in reciprocal lattice units are Γ: (0, 0, 0), C: (0.27, 0.27, 0), C_2: (-0.27, 0.73, 0), Y2: (-0.5, 0.5, 0), M_2: (-0.5, 0.5, 0.5), D:(-0.27, 0.73, 0.5), D_2: (0.27, 0.27, 0.5), A: (0, 0, 0.5), L_2: (0, 0.5, 0.5), and V_2: (0, 0.5, 0). (c) Depiction of the four segments (in green) that comprise of the full Brillouin Zone, Γ-C, C_2 -Y_2- Γ -M_2-D, D_2 -A-Γ, and L_2 -Γ-V_2, for $CuSn_2SI_3$. The figure includes views of the three-dimensional Brillouin zone from four different angles, to best visualise these segments.

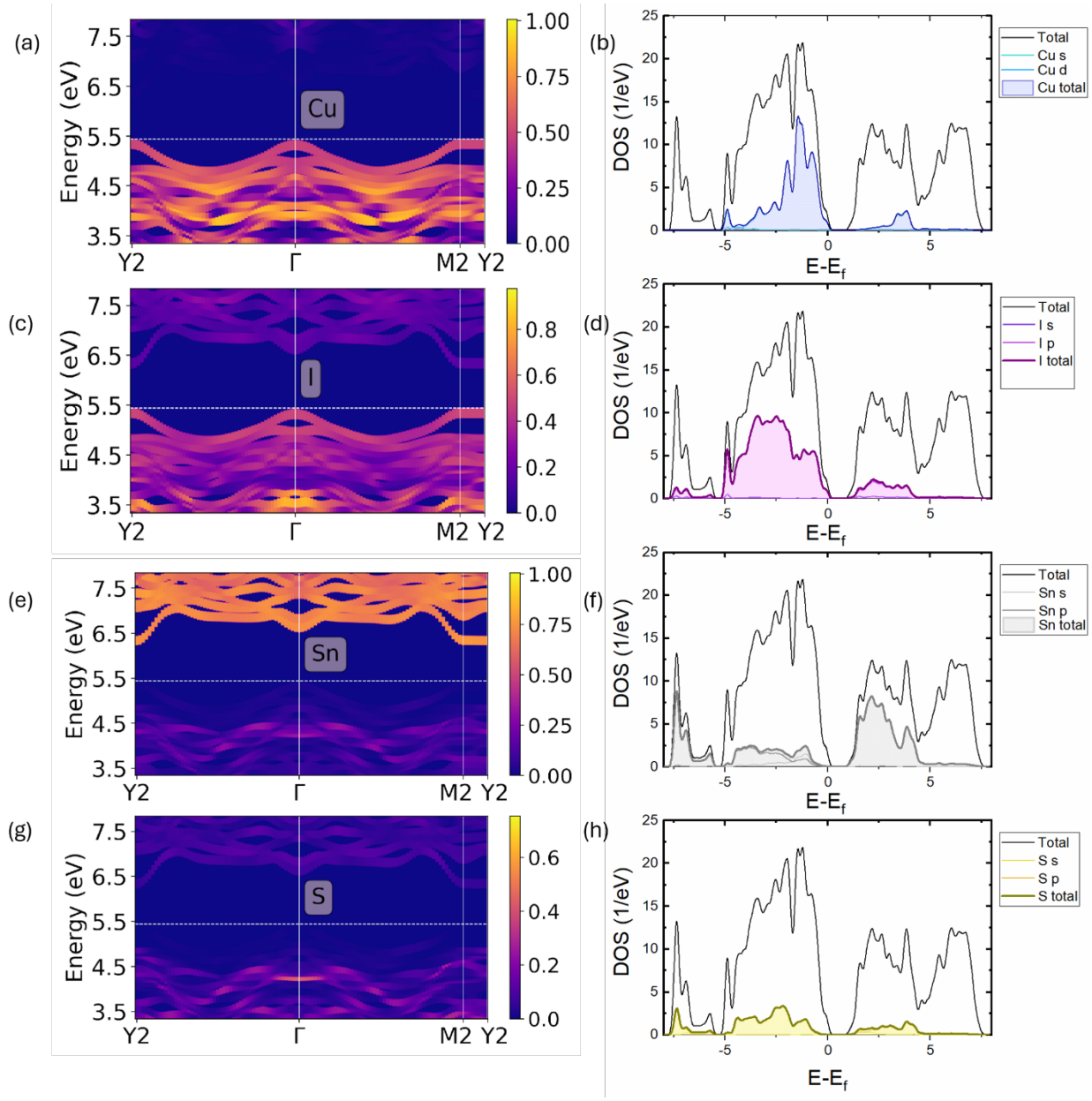

Figure S13 Density of states for the relaxed structure of $CuSn_2SI_3$ calculated using DFT(PBE)+SOC. Left panels: the k resolved DOS showing each elemental contribution. Right panels: The partial density of states with energy for the corresponding elements. The clear contribution to the VBT from Cu and I and from Sn to the CBB is seen.

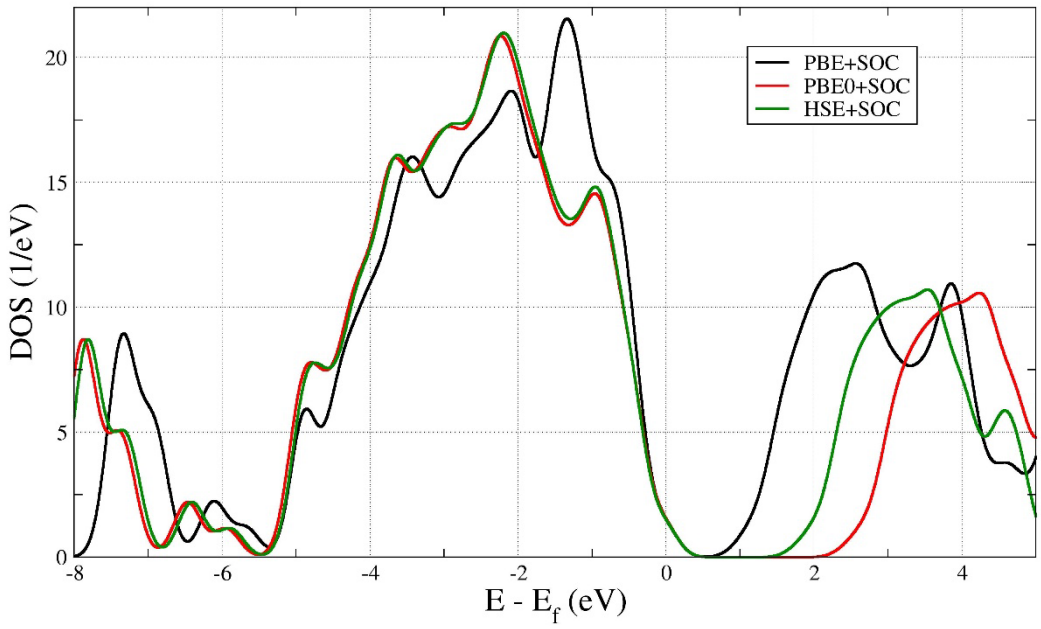

Figure S14 Comparison of the total density of states as obtained from DFT+SOC and the PBE0 and HSE hybrid functionals, using an experimentally motivated Gaussian broadening of 0.25 eV. Calculations were performed for the relaxed structure of $CuSn_2SI_3$.

Table S10. Comparison of lattice parameters between the reported experimental structure and the unconstrained volume relaxed structure with DFT (PBE), as well as bandgaps with PBE, PBE+SOC and Hybrid functionals

Structure	Lattice parameters						Method	Bandgap (eV)
	a (Å)	b (Å)	c (Å)	α (°)	β (°)	Γ (°)		
Experimental	7.340	7.340	14.440	96.775	96.775	34.139	Experiment	2.2
							PBE	0.962
							PBE + SOC	0.891
Unconstrained volume relaxation with DFT (PBE)	7.785	7.875	14.887	96.987	96.987	31.809	PBE	1.068
							PBE + SOC	0.996
							PBE0	2.452
							HSE	1.793

Measurement of charge-carrier mobility

Optical-pump Terahertz-probe (OPTP) spectroscopy setup

The OPTP setup used is this work is already described in detail elsewhere.[9–12] In short, an amplified Ti:sapphire laser system (Spectra-Physics Spitfire) is providing 800-nm centred ultrashort laser pulses with 5-kHz repetition and 35-fs pulse duration. The beam is subsequently split into 3 beams: probe, gate and pump. The first beam (probe) is used to generate single-cycle THz radiation pulses with a spintronic emitter (W/$Co_{40}Fe_{40}B_{20}$/Pt multilayer film on quartz) via the inverse spin Hall effect.[13] The second beam (gate) is used to detect THz radiation pulses by using free-space electro-optic sampling (EOS). Detection of the THz pulses with EOS is performed using a set of a 1-mm-thick (110)-ZnTe crystal, a quarter-wave plate, a Wollaston prism and a pair of balanced photodiodes. The third beam (pump) is used to photoexcite charge carriers within a semiconductor. For this, the 800-nm pulses are doubled in frequency with second harmonic generation in a beta-barium-borate (BBO) crystal to obtain 400-nm pulses. A short-pass filter was used to filter out the residual 800nm radiation. Subsequently, the semiconductor is photoexcited with these 400-nm pulses.

Extraction of charge-carrier mobility from optical-pump terahertz-probe spectroscopy

The relative change in the sample transmission of the THz pulse upon photoexcitation may be written as:

$$\frac{\Delta T}{T} = \frac{E_{S*} - E_S}{E_S} = \frac{E_{S*}}{E_S} - 1, \tag{S1}$$

where E_{S*} is the transmitted electric field of the terahertz pulse after the photoexcited material, and E_{S*} is the transmitted field after the non-photoexcited sample.

For highly absorbing materials, the thickness of the photoexcited layer (d_1) is much lower than the wavelength of the incident THz radiation ($d_1 = 1/\alpha \approx 1\mu m \ll \lambda_{THz}$, where α is the extinction coefficient of 400nm light). Therefore, equation (S1) may be expanded using the thin-film approximation, and the following expression can be obtained for the photoconductivity:[11,14]

$$\Delta\sigma(w) = -\frac{\varepsilon_0 c(n_1 + n_2)}{d_1}\frac{\Delta T}{T}, \tag{S2}$$

where d_1 is the thickness of the photoexcited layer, ε_0 is the vacuum permittivity, c is the speed of light, n_1 and n_2 are refractive indexes surrounding the photoexcited layer. In our case $n_1 \approx 1$ is the refractive index of vacuum, and $n_2 \approx 5.1$ is the refractive index of the bulk $CuSn_2SI_3$ pellet in the THz range, which was measured with THz time-domain spectroscopy (see details below).

The effective mobility of charge carriers can be obtained with:

$$\varphi\mu = \frac{\Delta S}{e n_{eff}} = \frac{\Delta\sigma d_1}{e n_{eff}}, \tag{S3}$$

where $\Delta S = \Delta\sigma d_1$ is the sheet photoconductivity, e is an elementary charge, n_{eff} is the effective areal density of charge carriers, accounting for the Gaussian intensity profiles of both the optical pump beam that excites the carriers and the terahertz probe beam, $\varphi\mu$ is the lower limit of the

electron-hole sum mobility, given that φ represents the photon-to-free-charge branching ratio and therefore ranges between 0 and 1. The value of n_{eff} is calculated as:

$$n_{eff} = \frac{E_{pulse}}{E_{photon}} \frac{1}{A_{eff}} (1 - R - T), \tag{S4}$$

where E_{pulse} is the energy of the photoexcitation pulse, E_{photon} is the energy of a corresponding photon of the central pulse wavelength (λ_{excit}), R and T are reflection and transmission coefficients for the central wavelength of the excitation pulse, A_{eff} is a parameter related to the effective overlap of excitation and terahertz beams at the sample position. The A_{eff} is derived as:[9,11]

$$A_{eff} = \frac{\pi}{4ln2} \left(\zeta_{pump}^2 + \zeta_{probe}^2\right), \tag{S5}$$

where ζ_{Vis} and ζ_{THz} are the full width at half maximum (FWHM) of the visible excitation and terahertz probe beams at the sample position, respectively. Substituting expressions S2, S4, S5 into equation S3 we obtain the final formula for calculating the effective mobility:

$$\varphi\mu = -\varepsilon_0 c(n_1 + n_2) \left(\frac{\Delta T}{T}\right) \frac{1}{e} \frac{E_{photon}}{E_{pulse}} \frac{\pi}{4ln2} \frac{\zeta_{pump}^2 + \zeta_{probe}^2}{(1 - R - T)}. \tag{S6}$$

We note that the sheet photoconductivity signal measured by OPTP originates from the combined contributions of photogenerated free electrons and holes. Consequently, the extracted charge-carrier mobility represents the sum mobility of electrons and holes.

Extraction of THz refractive index with time-domain THz spectroscopy

The extraction of the refractive index of a material in the terahertz range is possible using THz time-domain spectroscopy (THz TDS).[15] To achieve this, two measurements are necessary: the first measurement is the terahertz pulse profile without a sample in its path (reference), and the second is the transient passed through the sample. Additionally for samples where the thin-film approximation is invalid, it is necessary to measure the thickness.[15] We first consider the case of THz pulse propagation along the optical path from the emitter to the detector without a sample — the reference case. In this case, for the pulse arriving at the detector, the following expression can be written:

$$\widetilde{E}_{ref}(\omega) = \xi(\omega)\widetilde{E}_0(\omega) exp\left(\frac{i\omega l}{c}\right), \tag{S7}$$

where $\tilde{E}_0(\omega)$ is the electric field of the THz pulse generated by the THz emitter, l the length of the optical path, c is the speed of light, and $\xi(\omega)$ accounts for the interaction of the THz pulse with optical elements along the optical path. For a pulse additionally transmitted through a sample with a complex refractive index ($\tilde{n}_s(\omega) = n_s + i\kappa_s$):

$$\tilde{E}_s(\omega) = \xi(\omega)\tilde{E}_0(\omega) exp\left(\frac{i\omega(l-d)}{c}\right) T_{vs} T_{sv} exp\left(\frac{i\tilde{n}_s \omega d}{c}\right) FP_{vsv}(\omega) \tag{S8}$$

$$FP_{ijk}(\omega) = \sum_{p=0}^{N} \left[R_{jk} R_{ji} exp\left(\frac{2i\tilde{n}_s \omega d}{c}\right)\right]^p \tag{S9}$$

$$R_{ij} = (\tilde{n}_i - \tilde{n}_j)/(\tilde{n}_i + \tilde{n}_j) \tag{S10}$$

$$T_{ij} = 2\tilde{n}_i/(\tilde{n}_i + \tilde{n}_j). \tag{S11}$$

Here, d is the thickness of the sample, T_{vs} and T_{sv} are Fresnel transmission coefficients, R_{ij} are Fresnel reflection coefficients, FP_{vsv} are Fabry–Perot terms with N number of echoes. In (S8-S11)

indexes i, j and s, v are denoting the medium. For example, s stands for the sample medium and v for vacuum.

The complex transmission function of the terahertz pulse propagated through the sample can be obtained as the ratio of (S8) to (S7):

$$\tilde{T}(\omega) = \frac{\tilde{E}_s}{\tilde{E}_{ref}} = T_{vs}T_{sv}exp\left(\frac{i(\widetilde{n_s} - 1)\omega d}{c}\right)FP_{vsv}(\omega) \quad \text{(S12)}$$

In the case of a thick powder pressed into a pellet, the Fabry–Perot reflections can be filtered out by temporal windowing of the time-domain data. This truncates the Fabry–Perot summation after one term, i.e. $FP_{vsv}(\omega)$ = 1. Therefore, the expression (S12) transforms into:

$$\tilde{T}(\omega) = T_{vs}T_{sv}exp\left(\frac{i(\tilde{n}_s - 1)\omega d}{c}\right), \quad \text{(S13)}$$

from which the refractive index (real part) $n_s(\omega)$ and the extinction coefficient κ_s can be obtained:

$$n_s(\omega) = 1 + \frac{c}{\omega d}\arg\left(\tilde{T}(\omega)\right) \quad \text{(S14)}$$

$$\kappa_s(\omega) = -\frac{c}{\omega d}ln\left|\frac{\tilde{T}(\omega)}{T_{vs}T_{sv}}\right|, \quad \text{(S15)}$$

where $\tilde{T}(\omega)$ is measured experimentally. However, equations (S14) and (S15) are derived assuming real values of $\tilde{n}_{i,j}$ when calculating T_{ij} (S11), which is applicable only for low absorbing samples. For the case of a highly absorbing pellet, such as was measured in this study, the following system of equations should be used:

$$n_s(\omega) = 1 + \frac{c}{\omega d}\left\{\arg[\tilde{T}(\omega)] - \arg\left[\frac{4\tilde{n}_s}{(\tilde{n}_s + 1)^2}\right]\right\} \quad \text{(S16)}$$

$$\kappa_s(\omega) = \frac{c}{\omega d}\left\{ln\left|\frac{4\tilde{n}_s}{(\tilde{n}_s + 1)^2}\right| - \ln\left|\tilde{T}(\omega)\right|\right\}, \quad \text{(S17)}$$

which can be solved numerically. In this work we used a simple fixed-point iteration method[16] for solving (S16)-(S17) using $\tilde{T}(\omega) = \tilde{E}_s/\tilde{E}_{ref}$ measured experimentally. Figure (b) shows the refractive index of the $CuSn_2SI_3$ pellet extracted with the described method.

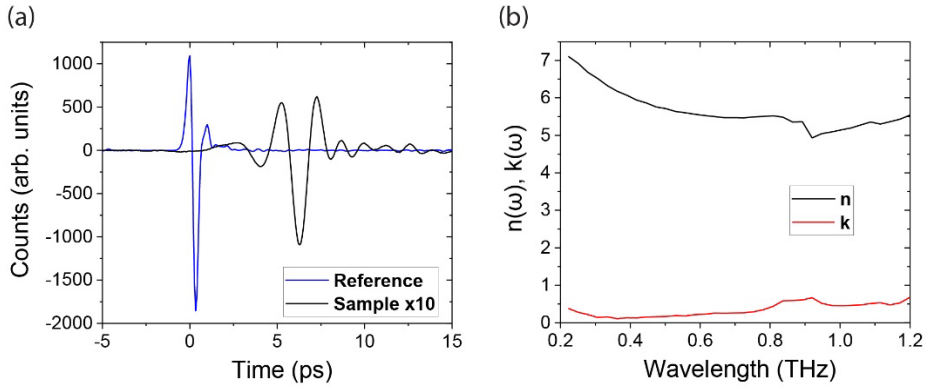

Figure S15 (a) THz pulse transient profiles recorded without and with the $CuSn_2SI_3$ pellet (thickness d=0.48 mm) in the beam path. (b) Extracted real (n) and imaginary (k) parts of the refractive index in the THz range.

The crystal structures of CuSn2SI3 (solved at 295 K) and Cu0.35Sn5.29S2I7 (solved at 100 K) are deposited with CSD accession codes 2503028 and 2503027, respectively.

Table S11 Crystal data and structure refinement for the compound $CuSn_2SI_3$ from single crystal XRD

Empirical formula	CuI_3SSn_2	
Formula weight	713.68	
Temperature	295(1) K	
Wavelength	0.71073 Å	
Crystal system	Monoclinic	
Space group	C 2/m	
Unit cell dimensions	a = 14.0334(5) Å	α= 90°.
	b = 4.3091(2) Å	β= 97.089(3)°.
	c = 14.4404(5) Å	γ = 90°.
Volume	866.55(6) $Å^3$	
Z	4	
Density (calculated)	5.470 Mg/m^3	
Absorption coefficient	18.982 mm^{-1}	
F(000)	1216	
Theta range for data collection	2.843 to 30.652°.	
Index ranges	-15<=h<=17, -6<=k<=5, -20<=l<=20	
Reflections collected	9698	
Independent reflections	1253 [R(int) = 0.0306]	
Completeness to theta = 26.32°	99.9 %	
Absorption correction	Empirical	
Max. and min. transmission	0.703 and 0.253	
Refinement method	Full-matrix least-squares on F^2	
Data / restraints / parameters	1253 / 0 / 43	
Goodness-of-fit on F^2	1.079	
Final R indices [I>2sigma(I)]	R1 = 0.0204, wR2 = 0.0484	
R indices (all data)	R1 = 0.0246, wR2 = 0.0505	
Largest diff. peak and hole	1.030 and -1.537 $e.Å^{-3}$	

Table S12 Single crystal XRD data for $CuSn_2SI_3$. Atomic coordinates and equivalent isotropic displacement parameters ($Å^2$). U(eq) is defined as one third of the trace of the orthogonalized U^{ij} tensor.

	x	y	z	U(eq)
I1	0.42846(3)	1.000000	0.35494(3)	0.02189(10)
I2	0.11979(3)	0.000000	0.19298(3)	0.02386(11)
I3	0.37934(3)	0.000000	0.06431(3)	0.02472(11)
Sn1	0.37298(3)	0.500000	0.52747(3)	0.02356(11)
Sn2	0.27961(4)	0.500000	0.24249(3)	0.02739(12)
Cu1	0.18998(7)	0.000000	0.02713(7)	0.0406(2)
S1	0.21759(10)	0.500000	0.40664(9)	0.0172(3)

Table S13 Anisotropic displacement parameters ($Å^2$) for $CuSn_2SI_3$ from single crystal XRD. The anisotropic displacement factor exponent takes the form: $-2\pi^2[h^2a^{*2}U^{11} + ... + 2\ h\ k\ a^*\ b^*\ U^{12}]$.

	U^{11}	U^{22}	U^{33}	U^{23}	U^{13}	U^{12}
I1	0.0221(2)	0.0200(2)	0.02344(19)	0	0.00220(14)	0.000
I2	0.0258(2)	0.0236(2)	0.02190(19)	0.000	0.00182(15)	0.000
I3	0.0280(2)	0.0240(2)	0.02243(19)	0.000	0.00437(15)	0.000
Sn1	0.0186(2)	0.0248(2)	0.0268(2)	0.000	0.00105(16)	0.000
Sn2	0.0372(3)	0.0259(2)	0.0202(2)	0.000	0.00802(18)	0.000
Cu1	0.0439(6)	0.0378(5)	0.0396(5)	0.000	0.0030(4)	0.000
S1	0.0190(7)	0.0191(7)	0.0135(6)	0.000	0.0028(5)	0.000

Table S14 Structural parameters from the Rietveld refinement of the powder XRD data at room temperature

Empirical Formula	$CuSn_2SI_3$
Crystal System	Monoclinic
Space group	C 2/m (12)
Unit cell parameters	a = 14.0369(1) Å b = 4.30723(5) Å c = 14.4467(1) Å β = 97.007(5) ˚
Cell volume	866.93(1) $Å^3$
Density	5.4684(8) g/cm^3
Rietveld R_{wp}	2.47 %
R_{exp}	0.33 %
R_p	1.54 %
gof	7.3715

Table S15 Atomic coordinates and isotropic displacement parameter from the Rietveld refinement of the powder XRD data for $CuSn_2SI_3$ at room temperature.

Site	x	y	z	Occupancy	U_{iso} (Å^2)
I1	0.42947	1	0.35397	1.0	0.015(1)
I2	0.12106	0	0.19262	1.0	0.0211(9)
I3	0.37965	0	0.06326	1.0	0.0199(9)
Sn1	0.37228	0.5	0.52767	1.0	0.0220(9)
Sn2	0.28012	0.5	0.24248	1.0	0.032(1)
Cu1	0.19009	0	0.02529	1.0	0.038(1)
S1	0.21539	0.5	0.41055	1.0	0.018(1)

Table S16 Structural parameters from the Rietveld refinement of the powder XRD data at 100 K.

Empirical Formula	$CuSn_2SI_3$ (100 K)
Crystal System	Monoclinic
Space group	C 2/m (12)
Unit cell parameters	a = 13.9581(1) Å b = 4.28099(3) Å c = 14.3988(1) Å β = 96.8993(5) ˚
Cell volume	854.17(1) Å^3
Density	5.5501(8) g/cm^3
Rietveld R_{wp}	2.71 %
R_{exp}	0.35 %
R_p	1.75 %
gof	7.76

Table S17 Atomic coordinates and isotropic displacement parameter from the Rietveld refinement of the powder XRD data for $CuSn_2SI_3$ at 100 K.

Site	x	y	z	Occupancy	U_{iso}(Å^2)
I1	0.42991	1	0.35380	1.0	0.0027(7)
I2	0.12243	0	0.19130	1.0	0.0059(6)
I3	0.38102	0	0.06420	1.0	0.0072(6)
Sn1	0.37254	0.5	0.52661	1.0	0.0092(7)
Sn2	0.28142	0.5	0.24171	1.0	0.0152(7)
Cu1	0.19037	0	0.02411	1.0	0.0105(9)
S1	0.21434	0.5	0.40869	1.0	0.002(1)

Table S18 Crystal data and structure refinement from single crystal XRD for the compound $Cu_{0.35}Sn_{5.29}S_2I_7$.

Empirical formula	$Cu_{0.35}$ I_7 S_2 $Sn_{5.29}$	
Formula weight	1602.53	
Temperature	100(2) K	
Wavelength	0.71073 Å	
Crystal system	Monoclinic	
Space group	C 2/m	
Unit cell dimensions	a = 14.1572(8) Å	α= 90°.
	b = 4.3847(2) Å	β= 110.303(7)°.
	c = 17.1829(11) Å	γ = 90°.
Volume	1000.36(11) $Å^3$	
Z	2	
Density (calculated)	5.320 Mg/m^3	
Absorption coefficient	17.855 mm^{-1}	
F(000)	1355	
Crystal size	0.079 x 0.007 x 0.004 mm^3	
Theta range for data collection	2.528 to 33.511°.	
Index ranges	-21<=h<=21, -6<=k<=6, -26<=l<=26	
Reflections collected	14206	
Independent reflections	2007 [R(int) = 0.0707]	
Completeness to theta = 25.242°	99.9 %	
Absorption correction	Analytical	
Max. and min. transmission	0.962 and 0.703	
Refinement method	Full-matrix least-squares on F^2	
Data / restraints / parameters	2007 / 0 / 60	
Goodness-of-fit on F^2	1.042	
Final R indices [I>2sigma(I)]	R1 = 0.0287, wR2 = 0.0641	
R indices (all data)	R1 = 0.0406, wR2 = 0.0699	
Extinction coefficient	0.00001(4)	
Largest diff. peak and hole	1.791 and -2.181 $e.Å^{-3}$	

Table S19 Atomic coordinates (× 10^4) and equivalent isotropic displacement parameters (Å^2 × 10^3). U(eq) is defined as one third of the trace of the orthogonalized U^{ij} tensor for $Cu_{0.35}Sn_{5.29}S_2I_7$.

	x	y	z	U(eq)
I(001)	1106(1)	15000	1264(1)	14(1)
I(002)	4511(1)	5000	2596(1)	18(1)
I(00)	7714(1)	5000	6185(1)	20(1)
Sn(1)	1197(1)	10000	-279(1)	15(1)
Sn(2)	2836(1)	10000	2256(1)	20(1)
I(3)	5000	0	5000	33(1)
Sn(00)	6162(1)	5000	4427(1)	28(1)
S(008)	3034(1)	10000	803(1)	13(1)
Cu(1)	7968(8)	5000	4721(6)	30(3)
Cu(2)	5788(9)	5000	5855(8)	30(4)

Table S20 Anisotropic displacement parameters (Å^2 × 10^3) for $Cu_{0.35}Sn_{5.29}S_2I_7$. The anisotropic displacement factor exponent takes the form: $-2\pi^2[h^2a^{*2}U^{11} + ... + 2hka^*b^*U^{12}]$

	U^{11}	U^{22}	U^{33}	U^{23}	U^{13}	U^{12}
I(001)	12(1)	12(1)	18(1)	0	6(1)	0
I(002)	14(1)	13(1)	23(1)	0	4(1)	0
I(00)	23(1)	21(1)	19(1)	0	9(1)	0
Sn(1)	10(1)	15(1)	22(1)	0	6(1)	0
Sn(2)	26(1)	19(1)	19(1)	0	12(1)	0
I(3)	24(1)	20(1)	61(1)	0	22(1)	0
Sn(00)	26(1)	30(1)	27(1)	0	8(1)	0
S(008)	11(1)	12(1)	14(1)	0	5(1)	0
Cu(1)	33(6)	36(6)	20(5)	0	9(4)	0

References

1 T. Nilges, S. Reiser, J. H. Hong, E. Gaudin and A. Pfitzner, Preparation, structural, Raman and impedance spectroscopic characterisation of the silver ion conductor $(AgI)_2Ag_3SbS_3$, *Phys. Chem. Chem. Phys.*, 2002, **4**, 5888–5894.

2 A. Pfitzner, $(CuI)_2 Cu_3 SbS_3$: Copper Iodide as Solid Solvent for Thiometalate ions, *Chem. – Eur. J.*, 1997, **3**, 2032–2038.

3 R. Blachnik, W. Buchmeier and H. A. Dreisbach, Structure of lead(II) dimercury(II) diiodide disulfide, *Acta Crystallogr. C*, 1986, **42**, 515–517.

4 R. Blachnik, K. Lytze and H. Reuter, A New Quaternary Chalcogenide Halide: Synthesis and Structure of $Hg_2SnS_2Br_2$, *J. Solid State Chem.*, 1996, **126**, 95–98.

5 M.-Y. Ran, S.-H. Zhou, W. Wei, B.-J. Song, Y.-F. Shi, X.-T. Wu, H. Lin and Q.-L. Zhu, Quaternary Chalcohalides $CdSnSX_2$ (X = Cl or Br) with Neutral Layers: Syntheses, Structures, and Photocatalytic Properties, *Inorg. Chem.*, 2021, **60**, 3431–3438.

6 W. Peng, L. Li, S. Yu, H. Zheng and P. Yang, Structure, binding energy and optoelectrical properties of p-type CuI thin films: The effects of thickness, *Appl. Surf. Sci.*, 2020, **502**, 144424.

7 M. Nakamura, S. Inagaki, Y. Okamura, M. Ogino, Y. Takahashi, K. Adachi, D. Hashizume, Y. Tokura and M. Kawasaki, Band structures in orientation-controlled CuI thin films under epitaxial strain, *Phys. Rev. B*, 2022, **106**, 125307.

8 R. Lu, Z. Li, L. Yue, L. Song, S. Fang, T. Liu, P. Shen, Q. Li, X. Jin and B. Liu, Significant enhancement in the photoelectronic properties of SnI4 via pressure-tailored phase engineering, *Mater. Today Phys.*, 2024, **42**, 101381.

9 C. Q. Xia, J. Peng, S. Poncé, J. B. Patel, A. D. Wright, T. W. Crothers, M. Uller Rothmann, J. Borchert, R. L. Milot, H. Kraus, Q. Lin, F. Giustino, L. M. Herz and M. B. Johnston, Limits to Electrical Mobility in Lead-Halide Perovskite Semiconductors, *J. Phys. Chem. Lett.*, 2021, **12**, 3607–3617.

10 M. Righetto, S. Caicedo-Dávila, M. T. Sirtl, V. J.-Y. Lim, J. B. Patel, D. A. Egger, T. Bein and L. M. Herz, Alloying Effects on Charge-Carrier Transport in Silver–Bismuth Double Perovskites, *J. Phys. Chem. Lett.*, 2023, **14**, 10340–10347.

11 C. L. Davies, J. Borchert, C. Q. Xia, R. L. Milot, H. Kraus, M. B. Johnston and L. M. Herz, Impact of the Organic Cation on the Optoelectronic Properties of Formamidinium Lead Triiodide, *J. Phys. Chem. Lett.*, 2018, **9**, 4502–4511.

12 L. R. V. Buizza, A. D. Wright, G. Longo, H. C. Sansom, C. Q. Xia, M. J. Rosseinsky, M. B. Johnston, H. J. Snaith and L. M. Herz, Charge-Carrier Mobility and Localization in Semiconducting Cu_2AgBiI_6 for Photovoltaic Applications, *ACS Energy Lett.*, 2021, **6**, 1729–1739.

13 T. Seifert, S. Jaiswal, U. Martens, J. Hannegan, L. Braun, P. Maldonado, F. Freimuth, A. Kronenberg, J. Henrizi, I. Radu, E. Beaurepaire, Y. Mokrousov, P. M. Oppeneer, M. Jourdan, G. Jakob, D. Turchinovich, L. M. Hayden, M. Wolf, M. Münzenberg, M. Kläui and T. Kampfrath, Efficient metallic spintronic emitters of ultrabroadband terahertz radiation, *Nat. Photonics*, 2016, **10**, 483–488.

14 P. Kužel and H. Němec, Terahertz conductivity in nanoscaled systems: effective medium theory aspects, *J. Phys. Appl. Phys.*, 2014, **47**, 374005.

15 S. K. E. Merchant& University of Oxford, degree granting institution. Terahertz spectroscopy of thin-film semiconductors , *University of Oxford*, 2010, print.

16 W. Withayachumnankul, B. Ferguson, T. Rainsford, S. P. Mickan and D. Abbott, Simple material parameter estimation via terahertz time-domain spectroscopy, *Electron. Lett.*, 2005, **41**, 800–801.

17 C. J. Hawkins, J. A. Newnham, B. Almoussawi, N. L. Gulay, S. L. Goodwin, M. Zanella, T. D. Manning, L. M. Daniels, M. S. Dyer, T. D. Veal, J. B. Claridge and M. J. Rosseinsky, Synthesis,

Structure, and Properties of $CuBiSeCl_2$: A Chalcohalide Material with Low Thermal Conductivity, *Chem. Mater.*, 2024, **36**, 4530–4541.
18 Jolm F. Moulder, William F. Stickle, Peter E.'Sobol, and Kennetlf D. Bomben, *Handbook of X-ray Photoelectron Spectroscopy*, Perkin-Elmer Corporation, USA, 1992.
19 T. J. Whittles, in *Electronic Characterisation of Earth-Abundant Sulphides for Solar Photovoltaics*, ed. T. J. Whittles, Springer International Publishing, Cham, 2018, pp. 175–213.